Journal of High Energy Physics, Gravitation and Cosmology, 2022, 8, 768-799
https://www.scirp.org/journal/jhepgc
ISSN Online: 2380-4335
ISSN Print: 2380-4327

The Origin of Cosmic Structures Part 4—Nucleosynthesis

J. C. Botke

Nogales, Arizona, USA
Email: jcbotke@gmail.com

How to cite this paper: Botke, J.C. (2022) The Origin of Cosmic Structures Part 4—Nucleosynthesis. *Journal of High Energy Physics, Gravitation and Cosmology*, **8**, 768-799.
https://doi.org/10.4236/jhepgc.2022.83053

Received: June 9, 2022
Accepted: July 25, 2022
Published: July 28, 2022

Abstract

In our original paper, we outlined a new model of nucleosynthesis which began when a small percentage of the vacuum energy was converted primarily into neutron-antineutron pairs but with a very small excess of neutrons. In this paper, we present a detailed study of that original idea. We show that immediately after their inception, annihilation and charge exchange reactions proceeded at a very high rate and after an interval of no more than 10^{-12} s, the matter/antimatter asymmetry of the universe and the present-day abundance of baryons had been established. The annihilations produced the high density of leptons critical for the weak interactions and the photons that make up the CMB. The model predicts a photon temperature in agreement with the present-day CMB value and also explains the origin of the CMB anisotropy spectrum. We also show how the nucleosynthesis density variations needed to explain all cosmic structures can resolve the difficulties that arise when trying to explain observed primordial element abundances in terms of a single-density universal model of nucleosynthesis.

Keywords

Nucleosynthesis, Early Universe, Time-Varying Curvature

1. Introduction

In our original paper describing a new model of cosmology [1], we outlined a new model of nucleosynthesis that is much simpler than the standard model while making many predictions that agree with observations. In particular, this model readily accounts for the matter/antimatter asymmetry of the universe which the standard model does not do. In our original study, we examined a range of possibilities and concluded that an annihilation model is the only one in which a very small violation of the standard model of QCD results in the un-

iverse we experience today. The basic idea is that there was no existence other than the vacuum up until the time of nucleosynthesis and that at a time of about 4.3×10^{-5} s, a small percentage of the vacuum energy was converted primarily into neutron and antineutron pairs but with an excess of 1 - 3 neutrons for every 10^8 pairs. Annihilation and charge exchange reactions proceeded at a very high rate and after an interval of about 10^{-12} s, the antibaryons had all been annihilated and the abundance of baryons had reached its present-day value. The annihilation and charge exchange reactions also produced the photons that became the CMB along with a high density of leptons and lepton neutrinos.

For this model to work, there must be a small violation of QCD that accounts for the neutron excess. Such a violation involving neutrons is not, however, without precedence. The issue, which is known as the "neutron enigma" [2] is that the half-life of free neutrons depends on how the half-live is measured. The upshot is that a small percentage of free neutrons decay without leaving behind a proton which is the inverse of our assumption that neutrons appeared out of the vacuum unaccompanied by an antineutron."

We separate the entirety of nucleosynthesis into three phases. We use the term "nucleosynthesis proper" to refer to the third phase during which the light elements were formed from an initial population of protons and neutrons. This phase began when the temperature of the photon gas dropped below the deuterium breakup energy. By $t = 0.135\,\mathrm{s}$, the p/n ratio had reached a value of $\mathrm{p/n} \approx 7.4$ or $\mathrm{p}/(\mathrm{p}+\mathrm{n}) \approx 0.88$ and nucleosynthesis was underway".

The first phase began when a small percentage of the vacuum energy (≈0.1% - 0.2%) converted into an initial population of neutrons and antineutrons with a small excess of neutrons. We are supposing that this occurred at the time that the vacuum energy density equaled the energy density of a neutron which would place it at a time of $t_n \approx 4.3\times10^{-5}\,\mathrm{s}$. During this phase, charge exchange reactions created the protons, and annihilation reactions both eliminated the antibaryons and created the CMB and the leptons. (Our original idea was that a cascade of weak interactions was responsible for the protons but that turned out to be wrong.) This phase proceeded very rapidly and ended after about 10^{-12} s. By then, all the antibaryons had been annihilated and the remaining population of neutrons and protons had stabilized with an abundance ratio very close to $\mathrm{p/n} = 1$.

This first phase was followed by an intermezzo during which the energy distributions of the various particles were rearranged, the remaining mesons from the various annihilation output channels decayed, and a large fraction of the neutrons were converted into protons via weak interactions.

2. Model

The basis of our analysis is a numerical simulation that follows the evolution of a set of particle types. To keep things simple and also because of constraints on simulation execution times, we limited the included types to protons, neutrons,

electrons, neutrinos, and photons and their antiparticles. With this set of particles, we were able to show that the annihilation model works.

What we did not include were the pions, kaons, and muons and their neutrinos that were produced by the annihilation reactions and, while their presence was of no consequence as far as the baryon evolution is concerned, they do play a critical role in the thermalization process. Because of their omission, we were not able to track the thermalization or the weak interaction-driven transition from a p/n ratio of about unity at the end of the first phase to the value of $\mathrm{p/n} = 7.4$ at the end of the second phase. In this study, these are secondary issues so for now, we just accept that thermalization did occur and that the weak interactions did change the proton/neutron abundance ratio. The reason they were omitted was that their inclusion would have increased the laptop simulation run times to the point of being impractical.

While the list of particle types is limited, the actual numbers of such particles are huge. We obviously could not track individual particles so some sort of simplification was necessary. The initial density of neutrons, for example, was $\approx 10^{41}$ m^{-3} and their energies range from near 0 up to $\approx 2m_nc^2 \approx 2$ GeV. Our solution was to split the population of each particle type into a series of kinetic energy bins and to consider the members of each bin to be a distinct type. Thus, neutrons with kinetic energies between KE_i and KE_{i+1} are considered to be one type of particle while neutrons in a different bin are considered to be a different type. Within each bin, all the members are considered to have the same energy, $KE_{<i>} = \left(KE_i + KE_{i+1}\right)/2$, and to have an isotropic 3-velocity distribution. As the simulation proceeds, the population of each of the bins changes but bin energies do not. The total number of particles is then the sum of the 9 generic types each multiplied by the number of bins assigned to each type. With a bin count of 12 for each type, for example, we end up with 108 different "particles."

The number of reactions becomes large since for a given generic reaction type, e.g. $\mathrm{n} + \mathrm{p} \to \mathrm{n} + \mathrm{p}$, each of the binned neutron particles must be reacted with each of the binned proton particles. If the input generic types of the reaction are different and each type has 12 bins, there are 12 distinct particle types for each generic type so there are $12 \times 12 = 144$ different reactions. For the case in which the input generic types are the same, e.g. $\mathrm{n} + \mathrm{n} \to \mathrm{n} + \mathrm{n}$, elimination of double counting reduces the number from N_{bins}^2 to $N_{bins}\left(N_{bins} + 1\right)/2$. Ultimately, the model includes 39 generic reactions so the total number of distinct reactions exceeds 5000 if each generic type has 12 bins. The reaction count, however, turns out to be of little consequence as far as the simulation run times are concerned. Instead, because the set of non-linear reaction equations is stiff in the extreme (we are simultaneously dealing with reaction rates ranging from 1 s^{-1} up to 10^{21} s^{-1}), the limiting performance factor is the total number of particle types since solving the stiff equations requires repeatedly inverting a $\left(9 \times N_{bins}\right) \times \left(9 \times N_{bins}\right)$ Jacobian matrix and unfortunately, this matrix is dense so it is not possible to employ sparse or banded matrix efficiencies.

To solve the set of reaction equations, we employ the non-linear predictor/corrector ODE solver called Lsoda which is available on the internet. We treat Lsoda as a black box that makes calls to a user-supplied "GetRates" routine. The input for the call is a vector containing the current predicted particle densities and the output is another vector containing the calculated rate of change of each particle's density.

3. Relativistic Kinematics

We will now consider the kinematics of a typical reaction. We need to allow for the randomness in the directions of both the reactant and product particles. To do so, we subdivided the particles according to a set of bins based on the angle between the particle 3-velocities. Because we are assuming that the particles are distributed uniformly in each bin, the population of input angle bins will be uniform. In principle, we should take into account the fact that most reactions are peaked in the forward direction but doing so would add greatly to the computational load without adding much to the quality of the results because we are averaging over such a huge number of particles and reactions. Instead, we will assume a uniform distribution which is equivalent to assuming hard-sphere scattering. The latter is commonly used with success in other simulation work based on, for example, the DSMC method.

The calculation for each pairing is a multi-step process. We define an x-axis to lie along the direction of the first particle. We then,

1) Select an angle bin from the list assigned to the second particle.

2) Boost both particles from the vacuum frame to the center-of-momentum (CM) frame. (The term "vacuum frame" refers to the frame in which the vacuum is at rest. We use that term instead of "lab" frame because the latter is generally taken to mean the frame in which one of the input particles is at rest.)

3) Compute the total CM kinetic energy of the pair and then the reaction rate based on the cross section for the reaction and the respective bin populations.

4) Distribute the reaction product particles into another set of angle bins still in the CM frame.

5) Boost back to the vacuum frame and determine the outgoing particle's kinetic energies in that frame.

6) Determine the energy bin that each of the angle-distributed output particles falls into.

7) Finally, adjust the densities of the particles in each bin and compute the density rates of change.

It is fortunate that almost all of the computations involving bin energies, cross sections, and allocations can be done before starting the simulation. During the simulation, at each time step, the current reaction rates are calculated based on the current bin populations and then the bin particle density rates are updated by multiplying the just calculated rates by the pre-computed allocation ratios.

We will now work through the details of the kinematics. Starting in the va-

cuum frame of the incident particles, we orient a coordinate system so that particle 1 moves along the x-axis and particle 2 moves in the x-y plane as shown in Figure 1.

Each particle's 3-momentum is denoted by p_i and $E_i = \sqrt{p_i^2 c^2 + m_i^2 c^4}$ will denote its total energy. The 4-vector is $\mathbf{p}_i = (E_i, \vec{p}_i)$. The 3-vectors are

$$\vec{p}_1 = (p_1, 0), \tag{3-1a}$$

$$\vec{p}_2 = (p_2 \cos(\theta), p_2 \sin(\theta)). \tag{3-1b}$$

The velocity of the center of momentum is given by

$$\vec{v}_{cm} = c\frac{\vec{p}_1 c + \vec{p}_2 c}{E_1 + E_2} \tag{3-2}$$

so

$$|\vec{v}_{cm}| = c\frac{S_{12}}{E_1 + E_2} \tag{3-3}$$

where

$$S_{12} = \sqrt{(p_1 c)^2 + (p_2 c)^2 + 2(p_1 c)(p_2 c)\cos(\theta)}. \tag{3-4}$$

The angle α is given by

$$\alpha = \tan^{-1}\left(\frac{(p_2 c)\sin(\theta)}{p_1 c + (p_2 c)\cos(\theta)}\right). \tag{3-5}$$

We next define a new coordinate system with the x'-axis aligned along $\vec{v}_{cm}$. The particle momenta in this new system are

$$\begin{aligned}\vec{p}_1' &= (p_1 \cos(\alpha), -p_1 \sin(\alpha)) \\ &= \frac{p_1}{S_{12}}(p_1 + p_2 \cos(\theta), -p_2 \sin(\theta))\end{aligned} \tag{3-6a}$$

$$\begin{aligned}\vec{p}_2' &= (p_2 \cos(\theta - \alpha), -p_2 \sin(\theta - \alpha)) \\ &= \frac{p_2}{S_{12}}(p_1 \cos(\theta) + p_2, p_1 \sin(\theta))\end{aligned} \tag{3-6b}$$

We now perform a boost from the vacuum frame to the CM frame along the x'-axis.

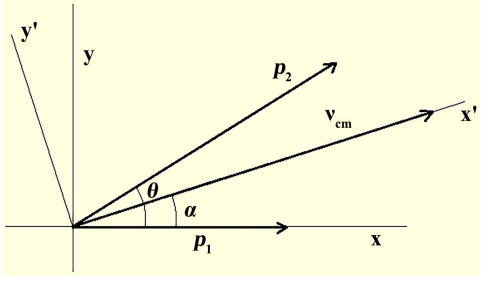

Figure 1. Particle momenta in the vacuum reference frame.

$$\begin{pmatrix} E_1^*/c \\ p_{1\|}^* \\ p_{1\perp}^* \\ 0 \end{pmatrix} = \begin{pmatrix} \gamma_{cm} & -v_{cm}\gamma_{cm}/c & . & . \\ -v_{cm}\gamma_{cm}/c & \gamma_{cm} & . & . \\ . & . & 1 & . \\ . & . & . & 1 \end{pmatrix} \begin{pmatrix} E_1/c \\ p_1\cos(\alpha) \\ -p_1\sin(\alpha) \\ 0 \end{pmatrix} \tag{3-7a}$$

$$\begin{pmatrix} E_2^*/c \\ p_{2\|}^* \\ p_{2\perp}^* \\ 0 \end{pmatrix} = \begin{pmatrix} \gamma_{cm} & -v_{cm}\gamma_{cm}/c & . & . \\ -v_{cm}\gamma_{cm}/c & \gamma_{cm} & . & . \\ . & . & 1 & . \\ . & . & . & 1 \end{pmatrix} \begin{pmatrix} E_2/c \\ p_2\cos(\theta-\alpha) \\ p_2\sin(\theta-\alpha) \\ 0 \end{pmatrix} \tag{3-7b}$$

From these, we obtain the relationships between the vacuum and CM frame energies and momenta.

$$E_1^* = \gamma\left(E_1 - \frac{c^2}{E_1+E_2}p_1\left(p_1 + p_2\cos(\theta)\right)\right), \tag{3-8a}$$

$$E_2^* = \gamma\left(E_2 - \frac{c^2}{E_1+E_2}p_2\left(p_1\cos(\theta) + p_2\right)\right), \tag{3-8b}$$

$$p_{1\|}^* = -p_{2\|}^* = \frac{p_1\left(p_1 + p_2\cos(\theta)\right)E_2 - p_2\left(p_1\cos(\theta)+p_2\right)E_1}{S_{12}\sqrt{\left(E_1+E_2\right)^2 - c^2\left(p_1^2+p_2^2+2p_1p_2\cos(\theta)\right)}}, \tag{3-8c}$$

$$p_{1\perp}^* = -p_{2\perp}^* = -\frac{p_1p_2}{S_{12}}\sin(\theta), \tag{3-8d}$$

$$p^* = \sqrt{\left(p_{1\|}^*\right)^2 + \left(p_{1\perp}^*\right)^2}. \tag{3-8e}$$

Figure 2 shows the momenta in the CM frame.

The angle between $\vec{p}_2^*$ and x'-axis is $\psi_{in}^* = \tan^{-1}\left(p_\perp^*/p_\|^*\right)$. This angle is the reference angle relative to which we define the angles ψ_{out}^* of the outgoing particles.

The momentum and energy of particle i are related to its velocity in the CM frame by

$$\vec{p}_i^* = \gamma_i m_i \vec{v}_i^*, \tag{3-9a}$$

$$E_i^* = \gamma_i m_i c^2. \tag{3-9b}$$

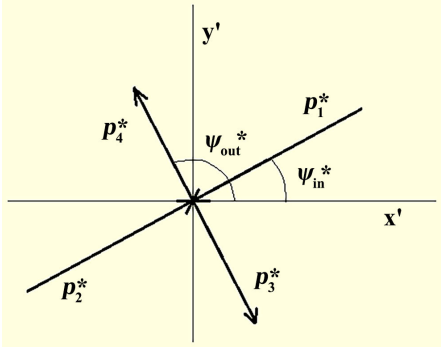

Figure 2. CM frame momenta.

Turning now to the reaction rate, at its simplest is given by

$$r = \sigma_{12}\rho_1\rho_2 \left| v_{rel} \right| \mathrm{m}^{-3} \cdot \mathrm{s}^{-1} . \tag{3-10}$$

The reaction rate is Lorentz invariant but the relativistic relative velocity given by

$$v_{rel} = \frac{v_1 + v_2}{1 + \frac{v_1 v_2}{c^2}} \tag{3-11}$$

is not. The densities, however, are also not Lorentz invariant but, as shown in [4], the product $\rho_1\rho_2 \left| v_{rel} \right|$ is Lorentz invariant and in the CM frame, has the value $\rho_{10}\rho_{20} \left| \vec{v}_1^{\,*} - \vec{v}_2^{\,*} \right|$ where the densities are the rest frame densities of the particles. The 3-velocity difference, given by

$$\frac{\left| \vec{v}_1^{\,*} - \vec{v}_2^{\,*} \right|}{c} = \frac{1}{c}\left| \frac{\vec{p}_1^{\,*}}{\gamma_1 m_1} - \frac{\vec{p}_2^{\,*}}{\gamma_2 m_2} \right| = \left(pc \right)^* \left(\frac{1}{E_1^*} + \frac{1}{E_2^*} \right) \tag{3-12}$$

can be greater than c, but since it is just a construct rather than a physical velocity, there is no violation of relativity.

The total CM energy is given by $E_1^* + E_2^*$ so the total CM kinetic energy (T^*) is

$$T^* = E_1^* + E_2^* - m_1c^2 - m_2c^2 . \tag{3-13}$$

The outgoing CM particle energies are

$$E_3^* = \sqrt{\left(p^* c \right)^2 + \left(m_3 c^2 \right)^2} , \tag{3-14a}$$

$$E_4^* = \sqrt{\left(p^* c \right)^2 + \left(m_4 c^2 \right)^2} . \tag{3-14b}$$

We now boost the outgoing particles back into the vacuum frame. The plane of the outgoing particles could be different from that of the incoming particles but that only amounts to a rotation about the x'-axis which would not affect the particle energies since the boost is along that axis. The equations are

$$\begin{pmatrix} E_3/c \\ p_{3,X} \\ p_{3,Y} \\ 0 \end{pmatrix} = \begin{pmatrix} \gamma_{cm} & +v_{cm}\gamma_{cm}/c & . & . \\ +v_{cm}\gamma_{cm}/c & \gamma_{cm} & . & . \\ . & . & 1 & . \\ . & . & . & 1 \end{pmatrix} \begin{pmatrix} E_3^*/c \\ p^* \cos\left(\psi_{out}^* - \pi \right) \\ p^* \sin\left(\psi_{out}^* - \pi \right) \\ 0 \end{pmatrix} \tag{3-15a}$$

$$\begin{pmatrix} E_4/c \\ p_{4,X} \\ p_{4,Y} \\ 0 \end{pmatrix} = \begin{pmatrix} \gamma_{cm} & +v_{cm}\gamma_{cm}/c & . & . \\ +v_{cm}\gamma_{cm}/c & \gamma_{cm} & . & . \\ . & . & 1 & . \\ . & . & . & 1 \end{pmatrix} \begin{pmatrix} E_4^*/c \\ p^* \cos\left(\psi_{out}^* \right) \\ p^* \sin\left(\psi_{out}^* \right) \\ 0 \end{pmatrix} . \tag{3-15b}$$

From these, we have

$$\begin{aligned} E_3 &= \gamma_{cm}\left(E_3^* - v_{cm} p^* \cos\left(\psi_{out}^* \right) \right) \\ &= \gamma_{cm}\left(E_3^* - v_{cm}\sqrt{E_3^{*2} - \left(m_3 c^2 \right)^2} \cos\left(\psi_{out}^* \right) \right) \end{aligned} \tag{3-16a}$$

$$\begin{aligned} E_4 &= \gamma_{cm}\left(E_4^* + v_{cm}p^*\cos\left(\psi_{out}^*\right)\right) \\ &= \gamma_{cm}\left(E_4^* + v_{cm}\sqrt{E_4^{*2} - \left(m_4c^2\right)^2}\cos\left(\psi_{out}^*\right)\right) \end{aligned} \tag{3-16b}$$

We are only interested in the outgoing energies so these results are all that we need. All these equations are expressed in terms of total energies and momenta so they are valid for both massive and zero mass particles.

For the binary reactions, we perform the series of steps outlined above. This process is very fast even with more than 5000 reactions. In the case of the neutron/antineutron decay reactions, there is no vacuum frame angle so we boost to the neutron's or antineutron's CM (rest) frame. We then assume that the proton/antiproton has the same energy as the neutron/antineutron so it is created at rest in the CM frame. We then assign the mass difference energy to the electron and neutrino or their antiparticles taking into account their different masses and distribute them into the possible output angles bins. Afterward, we boost back to the vacuum frame.

The baryon annihilation reactions present another variation. Ultimately, these result in photons, electrons/positrons, and their neutrinos but the reactions reach that final state by first producing mesons which then decay into the final particles. As far as the kinematics are concerned, we follow the binary reaction procedure under the assumption that the output particles are pions. We then take an extra step in which we boost into each pion's CM frame, allow the meson to decay into another set of angle bins, and then boost the lot back into the reaction CM frame. We now have four or more product particles. Finally, we boost everything back into the vacuum frame.

As noted earlier, the critical bottleneck of the simulation is the time needed to invert the Jacobian matrix. On our laptop, with 108 particle types, about 35 seconds is needed for each inversion, and increasing the number of types increases the total execution time more rapidly than by N^2.

We now wish to establish an appropriate simulation time scale. Each reaction is limited to a single value of kinetic energy. The number of reactions per second per unit comoving volume, $V(t)$, is given by

$$r = \sigma_{12}\frac{n_1}{V(t)}\frac{n_2}{V(t)}\left|\vec{v}_1^* - \vec{v}_2^*\right| \tag{3-17}$$

where n_1 and n_2 are the current numbers of particles in the respective bins. At the start of the simulation, the initial neutron and antineutron densities are on the order of 10^{41} and, as we will see shortly, the initial relative velocity is on the order of 10^6 m·s^{-1}. Assuming a representative cross section of 10 mb, we find a reaction rate of 10^{58} m^{-3}·s^{-1} so the rate per particle is on the order of 10^{17} m^{-3}·s^{-1}. For the simulation to work, we must define simulation time so that the reaction rates multiplied by the simulation time step are small. To accomplish this, we define a dimensionless time τ by

$$\frac{t}{t_n} \equiv 1 + \frac{\tau - 1}{10^{18}}. \tag{3-18}$$

The time $t_n = 4.3\times10^{-5}\,\mathrm{s}$ is the time at which the vacuum energy density equaled $m_n c^2$. In terms of τ, the reaction rate is

$$\frac{\mathrm{d}R}{V(\tau)\,\mathrm{d}\tau} = \sigma_{12}\frac{n_1}{V(\tau)}\frac{n_2}{V(\tau)}\left|\vec{v}_1^{\,*} - \vec{v}_2^{\,*}\right|\frac{t_n}{10^{18}}. \tag{3-19}$$

Next, to avoid dealing with large particle numbers, we define scaled values by $n_i = n_{0,n} n_{s,i}$ where $n_{0,n}$ is the initial number of neutrons in a volume of 1 m^3, and finally, we run the simulations in $\log_{10}$ time instead of linear time so we have

$$\frac{\mathrm{d}R_s}{V(s)\,\mathrm{d}s} = \left(\sigma_{12}\left|\vec{v}_1^{\,*} - \vec{v}_2^{\,*}\right|\frac{t_n n_{0,n}}{10^{18}}\ln(10)\right)\tau\frac{n_{s,1}}{V(s)}\frac{n_{s,2}}{V(s)} \tag{3-20}$$

where $\tau = 10^s$. In principle, the volume changes with time as a result of the expansion of the universe but in this case, the entire process occurs so quickly that the volume is constant.

The last step is to estimate the initial velocities of the neutrons and antineutrons. A lower bound is given by the uncertainty relation. Assuming an initial density of 10^{41} m^{-3} each for the neutrons and antineutrons, the average distance between particles is

$$\langle d\rangle = 2\left(\frac{3}{4\pi\times2\times10^{41}}\right)^{1/3} = 2.1\times10^{-14}\,\mathrm{m}. \tag{3-21}$$

Momentum uncertainty gives $\langle p\rangle = 2.6\times10^{-21}\,\mathrm{kg\cdot m\cdot s^{-1}}$ so $\langle v\rangle = 1.6\times10^{6}\,\mathrm{m\cdot s^{-1}}$ and $\langle KE\rangle = 3\left(\langle p\rangle^2/2m_n\right) = 0.04\,\mathrm{MeV}$. If we assume instead an initial density of 10^{42} m^{-3}, the velocity doubles, and kinetic energy increases by a factor of 4.

4. Reactions and Cross Sections

In Table 1, we list the reactions included in the simulation. The list was compiled by forming all the possible combinations of the 9 included particles.

Because of our bin model and the kinematics described in the previous section, we need the cross sections for all of these in the energy range, $0.1\,\mathrm{MeV} \le T^* \le 4000\,\mathrm{MeV}$. In some cases, extrapolations were necessary because of a lack of measured cross sections.

In all the figures that follow, we use the CM kinetic energy as the independent variable. It is common practice among experimentalists, however, to plot results using the lab momentum of the incident particle as the independent variable and in those cases, our figures will not match the referenced figures in appearance.

We will now work through the list of needed cross sections beginning with the baryon annihilations.

4.1. The $\mathrm{p}+\bar{\mathrm{p}}\to\mathrm{m}+\mathrm{m}$ and $\mathrm{n}+\bar{\mathrm{n}}\to\mathrm{m}+\mathrm{m}$ Reactions

The authors of [5] report the measurement of the $\mathrm{p}\bar{\mathrm{p}}$ reaction in the kinetic

energy range from about 8 MeV to 90 MeV. The authors did a fit to the measured cross sections that we used in the measured energy range but, because we were unable to locate results over a larger range of energies, we found it necessary to extrapolate in both directions. The result is shown in Figure 3.

We used the author's formula to extrapolate to low energies. For the large energies, we assumed the logarithmic form

$$\sigma(pc) = 10^{a\log_{10}(pc)+b} \tag{4-1}$$

Table 1. List of reactions included in the simulation.

Baryon Annihilation	Weak	Lepton Ann. & Prod.	Baryon Elastic
$n+\bar{n}\to m+m$	$n\to p+e^-+\bar{\nu}_e$	$e^-+e^+\rightleftharpoons\gamma+\gamma$	$n+n\to n+n$
$p+\bar{p}\to m+m$	$\bar{n}\to\bar{p}+e^++\nu_e$		$n+p\to n+p$
$n+\bar{p}\to m+m$		Lepton Elastic	$n+\bar{n}\to n+\bar{n}$
$\bar{n}+p\to m+m$	$n+e^+\rightleftharpoons p+\bar{\nu}_e$	$e^-+e^-\to e^-+e^-$	$n+\bar{p}\to n+\bar{p}$
	$\bar{n}+e^-\rightleftharpoons\bar{p}+\nu_e$	$e^++e^+\to e^++e^+$	$\bar{n}+\bar{n}\to\bar{n}+\bar{n}$
Charge Ex.	$n+\nu_e\rightleftharpoons p+e^-$	$e^-+e^+\to e^-+e^+$	$\bar{n}+\bar{p}\to\bar{n}+\bar{p}$
$p+\bar{p}\rightleftharpoons n+\bar{n}$	$\bar{n}+\bar{\nu}_e\rightleftharpoons\bar{p}+e^+$	$e^-+p\to e^-+p$	$p+p\to p+p$
		$e^-+\bar{p}\to e^-+\bar{p}$	$p+\bar{p}\to p+\bar{p}$
	Compton Scatt.	$e^++p\to e^++p$	$p+\bar{n}\to p+\bar{n}$
	$e^-+\gamma\to e^-+\gamma$	$e^++\bar{p}\to e^++\bar{p}$	$\bar{p}+\bar{p}\to\bar{p}+\bar{p}$
	$e^++\gamma\to e^++\gamma$		
	$p+\gamma\to p+\gamma$		
	$\bar{p}+\gamma\to\bar{p}+\gamma$		

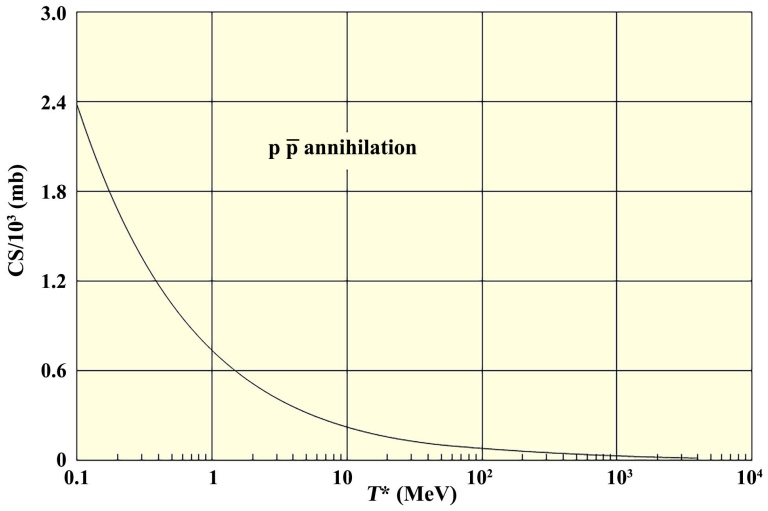

Figure 3. Total $p\bar{p}$ annihilation cross section.

where pc is the momentum of the incident particle in the lab frame. To fix the parameters, we required the formula to match the data at two points near the upper end of the measured energy range.

This reaction proceeds through several output channels. To simplify things, we assumed that the output was a mix of $\pi^0\pi^0$ and $\pi^+\pi^-$. We assumed that the neutral pions decayed directly into photons. The lifetime of $\pi^0 \to 2\gamma$ is 8.5 $\times 10^{-17}$ s so the neutral pions would have disappeared relatively rapidly. Had the charged pions decayed, they would have first decayed into muons and neutrinos and subsequently into electrons and neutrinos. The lifetimes of these decays are relatively long (2.6×10^{-8} s and 2.2×10^{-6} s respectively) so a more likely output channel was $\pi^+ + \pi^- \to 2\gamma$. The cross section for this reaction is about 10^7 larger than the weak interaction cross section so this output channel would have been a significant factor considering the very high density of the particles. With these assumptions, the end product of these reactions was 4 photons without any neutrinos. Ultimately, no matter what the branching ratios had been, the result would be the same; it is only a matter of how long it takes to get there.

We were unable to locate cross section data for the $n\bar{n}$ annihilation reaction so we just assumed that the cross sections were the same as for the $p\bar{p}$ reaction.

4.2. The $n + \bar{p} \to m + m$ and $\bar{n} + p \to m + m$ Reactions

We next consider the $n + \bar{p} \to m + m$, $\bar{n} + p \to m + m$ reaction pair. The review article [6] lists the results for the $\bar{n}p$ reaction which covers an energy range similar to that of the previous annihilation reactions. We did a fit to the data with the result that

$$\sigma(pc) = -133.2 + \frac{25.8}{pc} + 1436.9(pc) - 2485.7(pc)^2 \qquad (4\text{-}2)$$

where pc is the momentum of the incident particle in the lab frame. The extrapolation to larger energies was done using (4-1). The result is shown in Figure 4

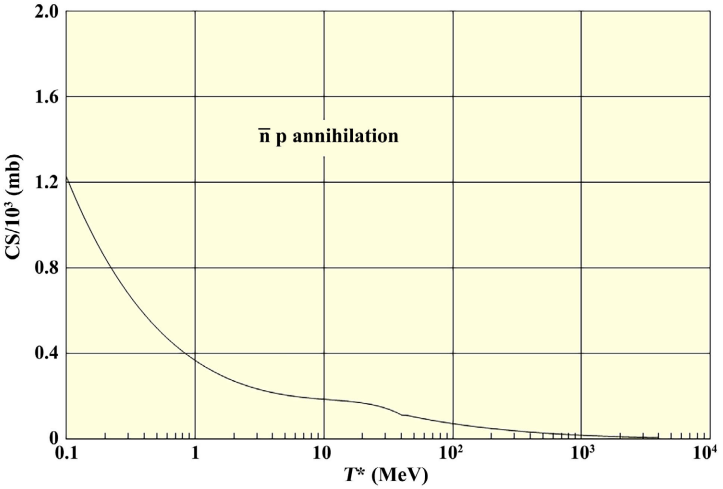

Figure 4. Total $\bar{n}p$ annihilation cross section.

In this case, we assumed that the output would be $\pi^+\pi^0$. As before, we assumed that the π^0 decayed into 2 photons. The charged pions, on the other hand, individually would have decayed ultimately to positrons/electrons and neutrinos but if we take these two reactions together, we again have pairings such as $\pi^+ + \pi^- \to 2\gamma$. In this case, however, we chose to assume the decay channel to get some idea of what the final neutrino densities might be. The charged pions decay into muons plus muon neutrinos. The muons then decay into an electron or positron plus an electron neutrino which leaves us with an electron/positron plus 2 neutrinos. We need to account for the extra neutrino but instead of further complicating the kinematics, we just doubled the number of output electron neutrinos.

As was the case for the previous reaction pair, we were unable to locate data for the $n\bar{p}$ annihilation reaction so we assumed it was the same.

4.3. Baryon Charge Exchange Reactions

The baryon charge exchange reactions are next. The available data for the $p\bar{p}$ reaction covers the same energy range [6] [7] [8] [9]. **Figure 5** shows the cross section.

We again used the procedure (4-1) for the large energy extrapolation. The solid line is the result of a cubic spline fit to the data.

We did not locate any measured cross sections for the $n\bar{n}$ charge exchange reaction. We expect that the strong drop in the $p\bar{p}$ cross section for small energies is a consequence of the proton-neutron mass difference and because there would not such barrier in the $n\bar{n}$ case, we extrapolated to small energies with a linear fit to all the data using the form $\sigma = a(pc) + b$. Otherwise, we assumed that the cross sections would be the same. The result is shown in **Figure 6**.

The extrapolation does not look like a linear fit to the data points in the figure but that is because we are plotting against the kinetic energy rather than the lab momentum of the incident particle and the kinetic energy axis is logarithmic.

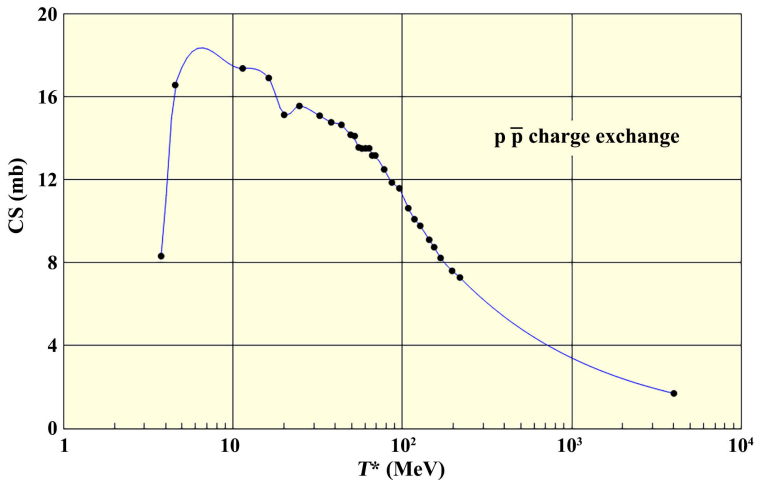

Figure 5. $p\bar{p}$ charge exchange cross section.

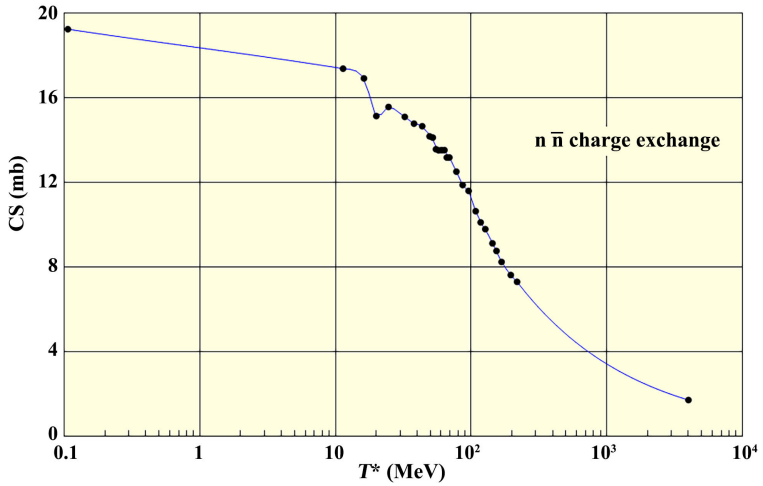

Figure 6. $n\bar{n}$ charge exchange cross section.

4.4. Weak Interactions

The first two weak reactions are the neutron and antineutron decay reactions. Despite the very high particle densities, these do not make a noticeable contribution during the period covered by the first phase of nucleosynthesis.

The authors of [10] report measurements of the charged current quasi-elastic (CCQE) neutrino cross sections which are shown in **Figure 7**.

The neutrino reaction situation is complex and we did not make any attempt to do it justice. It is well known that the cross sections for υN reactions are about twice as large as for the $\bar{\upsilon} N$ reactions at least for energies above 1 GeV, [11]. For the simulation, we assumed the single curve shown for all the reactions but multiplied by 1/2 for the $\bar{\upsilon} N$ reactions. We are only concerned with the relative importance of the neutrino reactions so while this is certainly an approximation, it will enable us to establish the point in time at which the weak interactions started to become significant.

4.5. Compton Scattering

The Klein-Nishina formula for the Compton scattering cross section is well known. See e.g. [12]. The $p^{\pm}\gamma$ reactions are included along with the $e^{\pm}\gamma$ reactions even though the cross section for the former is much smaller. At very low CM energies, the reaction rates of the latter are several orders of magnitude larger than those of the $p^{\pm}\gamma$ reactions but for larger energies, the differences are much smaller.

4.6. Lepton Pair Production and Annihilation

The cross section formulas for the two reactions can be found in [13].

4.7. Lepton Elastic Scattering

The $e^- + e^- \to e^- + e^-$ and $e^+ + e^+ \to e^+ + e^+$ reactions are known as Møller scattering. The formula for the differential cross section can be found in [14].

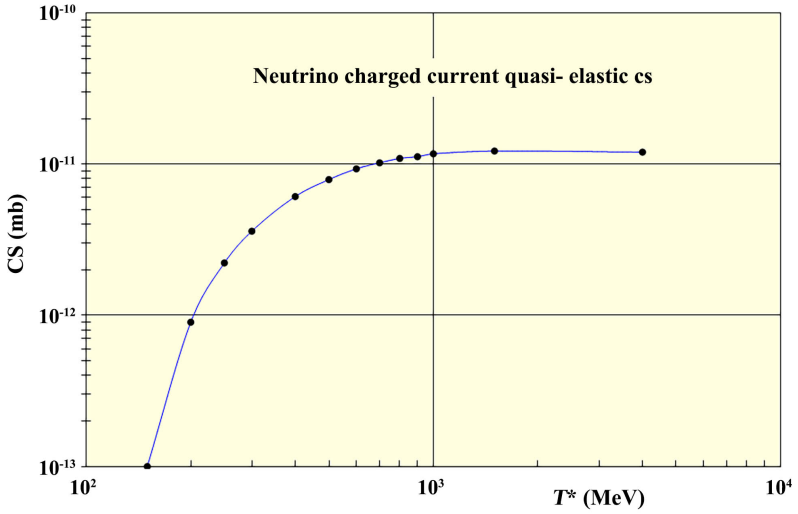

Figure 7. Neutrino charged current quasi-elastic cross sections.

The $e^- + e^+ \to e^- + e^+$ reaction is known as Bhabha scattering and has the same differential cross section as Møller scattering.

In the simulation, we need the total cross sections and integrating the differential cross section to obtain the totals requires the introduction of a small angle cutoff. We ran simulations with several cutoff values and found only very minor differences in the results.

The $e^\pm + p^\pm \to e^\pm + p^\pm$ reactions are known as Mott scattering. The cross section formula is given in [15].

4.8. Baryon Elastic Scattering

The low-energy nucleon elastic cross sections are discussed in [16]. The $n + n \to n + n$, $p + p \to p + p$ (and hence $\bar{n} + \bar{n} \to \bar{n} + \bar{n}$, and $\bar{p} + \bar{p} \to \bar{p} + \bar{p}$) elastic scattering are constant with a value of $\sigma = 25$ mb. The cross sections for the $n + p \to n + p$ reaction show a decline from 33 mb at an incident neutron energy of 380 MeV to 26 mb at 580 MeV. We assumed a linear variation with CM kinetic energy below 270 MeV (incident energy = 580 MeV.) In [17], the authors report differential cross sections at CM energies of 2.4 GeV that are similar to those of [16] from which we conclude that it is reasonable to assume that the cross sections are constant above 580 MeV incident energy.

For the $p + \bar{p} \to p + \bar{p}$, we used the data from [18]. We did a fit to the data with the result $\sigma = 41.1 + 488.4/T^* - 0.01T^*$ mb. Because of the similarity between the other reaction's particle to antiparticle replacement results, we assumed that the cross sections for $n + \bar{n} \to n + \bar{n}$, $n + \bar{p} \to n + \bar{p}$, and $p + \bar{n} \to p + \bar{n}$ could reasonably be presumed to be the same.

An important point concerning these reactions is that all the cross sections are on the order of 25 - 35 mb and that they only contribute towards the thermalization of the baryons so small errors in the cross sections will not affect the general character of the simulation results.

5. Results

In Figure 8 we show the results for a simulation done with a starting density of $n_n(0) = 10^{41}\ \mathrm{m}^{-3}$, a neutron excess of 2.0 × 10^{-8}, and a lepton elastic scattering cutoff angle of π/10.

Each generic particle was subdivided into 12 energy bins. The first bin has a width of 0.1 MeV and its only purpose is to hold the initial populations of neutrons and antineutrons. The range from 0.1 MeV to 1500 MeV was divided into 10 bins of equal width. Finally, one last bin with a width of 500 MeV was included to extend the range up to 2000 MeV. Not all of the bins are populated during the simulation but their presence is necessary to satisfy the kinematic constraints. The curves for the photons and leptons are shown dashed to remind the reader of the uncertainties associated with the products of the baryon annihilation reactions.

We see that the results justify our contention that an initial state consisting of only neutrons and antineutrons with a small bias in favor of neutrons can explain the matter/antimatter asymmetry, the present-day average baryon density, and the existence of the CMB. The reactions proceed rapidly and 10^{-12} s after the formation of the initial particles, the process is largely complete. The antibaryons are gone and the p/n ratio had stabilized at a value close to unity. The total baryon density at $\tau = 10^{12}$ is $\rho_{Sim} = 2\times10^{33}\ \mathrm{m}^{-3}$ which we compare with the value $\rho(t_n) = 3.9\times10^{33}\ \mathrm{m}^{-3}$ obtained by scaling the present-day average density $\rho(t_0) = 1\ \mathrm{m}^{-3}$.

Next, we will look at the particle energy distributions. In Figure 9, we show the energy distribution of the neutrons for four different values of τ.

Initially, the neutrons were limited to the very narrow first bin whose width was 0.1 MeV. Very quickly, the reactions induced a redistribution of the neutrons into the higher energy bins, and by $\tau = \tau_5$, the population was approaching a uniform distribution which it did reach by $\tau = \tau_{10}$. From that point onwards, the calculated distribution temporarily ceased to change. There is no indication yet of a developing shift away from a p/n ratio of unity but we will resolve that issue in Section 6. There is also no indication of thermalization developing, a problem which we will discuss in Section 8. The distributions for the antineutrons are essentially identical to those of the neutrons for the first three values of τ but by $\tau = \tau_{10}$, the density of the antineutrons had dropped below that of the neutrons by many orders of magnitude thus realizing the baryon/anti baryon asymmetry of the universe.

Figure 10 shows the corresponding results for the protons.

The initial density of protons was zero so the peak magnitudes are initially lower but we see that the protons were distributed to the higher energy bins more rapidly than were the neutrons. By $\tau = \tau_{10}$, the curves are the same. As was the case for the neutrons, the antiproton distributions were identical to the proton distributions up until the time that their density began its rapid decline.

The photon distributions are shown in Figure 11.

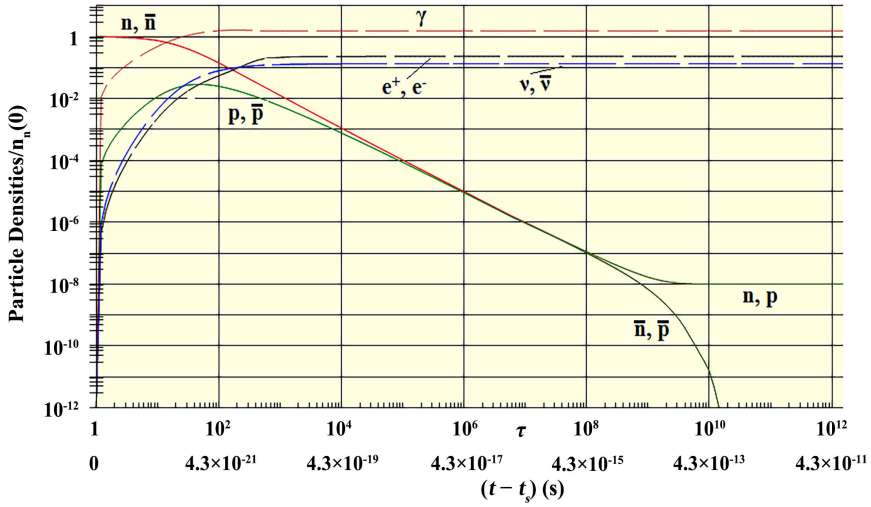

Figure 8. Simulation results with an initial neutron density $n_n(0) = 10^{41}\ \mathrm{m}^{-3}$ and a neutron excess of 2.0×10^{-8}.

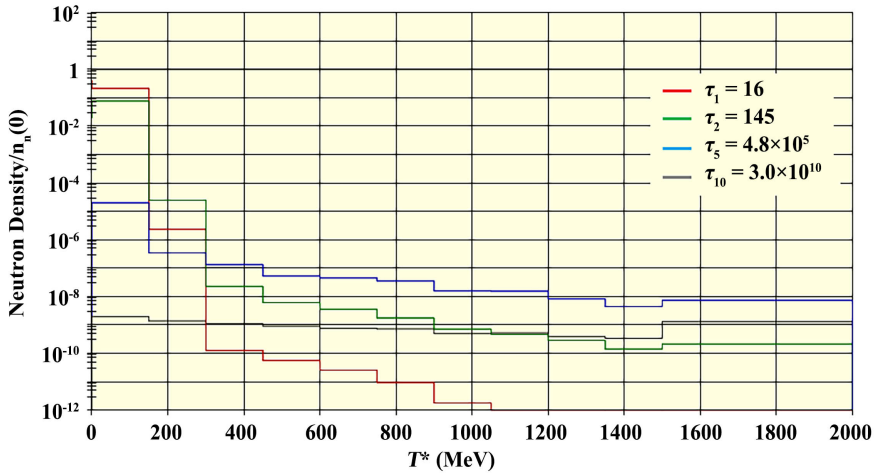

Figure 9. Neutron energy distributions for four values of τ.

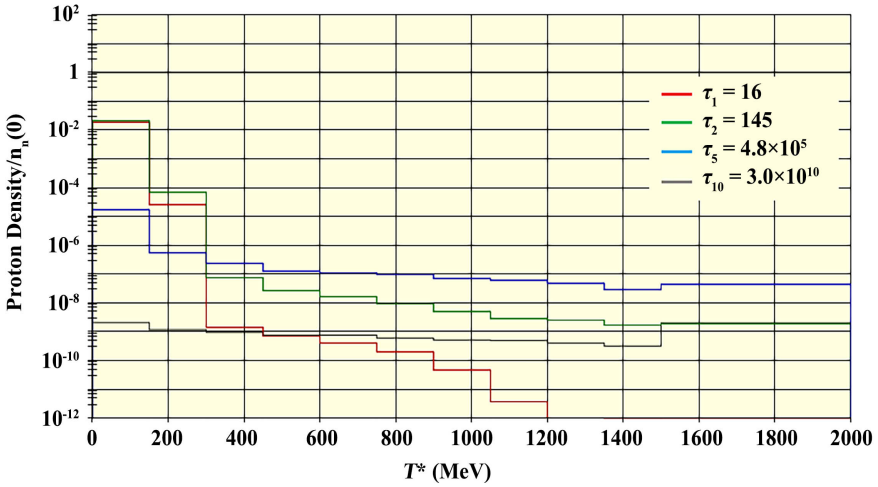

Figure 10. Proton energy distributions for four values of τ.

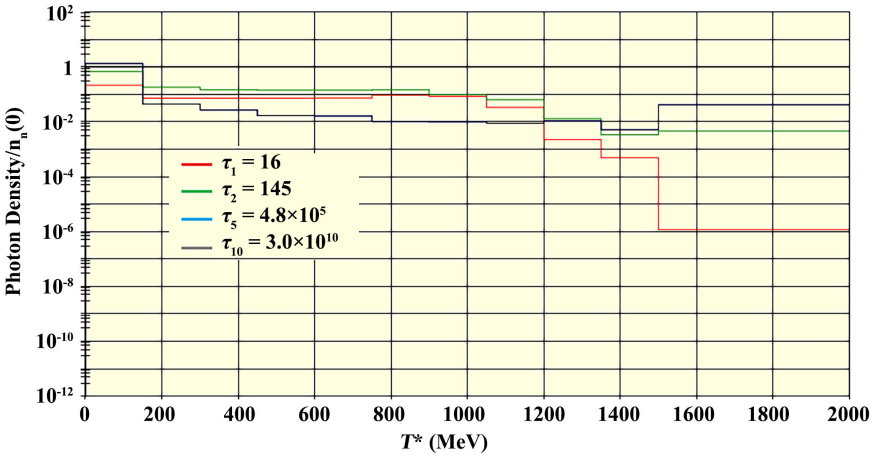

Figure 11. Photon energy distributions for four values of τ.

Again, there were no photons initially but as a consequence of the baryon annihilation reactions, their density increased rapidly and they very quickly approached a uniform distribution. There is some uncertainty about the actual density during the early stages because of our uncertainty concerning the annihilation branching ratios and the meson annihilation versus meson decay branching ratios. The initial densities were likely somewhat smaller but by $\tau = \tau_{10}$, the predicted density is probably not in error by a significant amount. We will discuss the CMB further in Section 8.

Because the photons are a *product* of the principal set of reactions rather than an active participant, errors in the predicted density do not affect the baryon density predictions.

In Figure 12, we show the electron distributions.

We see that the electron (and positron) distributions are biased towards the higher energies more so than are the photon distributions. This is a consequence of the various elastic scattering reactions as well as of the $e^{\pm}p^{\pm}$ reactions. The reaction rates for the lepton scattering and $e^{\pm}\gamma$ reactions remain very high throughout the time range considered which means that the photons and electrons/positrons would rapidly adjust to any change in the average temperature of the system. As is the case with the photons, the electrons and positrons are products of the principal baryon reactions and do not influence the baryon density predictions.

Finally, we consider the neutrinos distributions which are shown in Figure 13.

In this case, we see that the neutrino distributions remain confined to the lower energies because of the lack of any elastic neutrino reactions. By assumption, the large number of neutrinos is entirely a consequence of the $n\overline{p}$ and $\overline{n}p$ annihilation reactions. There is uncertainty about the actual total because of the aforementioned branching ratio problem but the prediction will be fractionally wrong rather than wrong by orders of magnitude. The weak reactions do become important later and for that to happen, a very large number of both

neutrinos and electrons/positrons is critical because of the very small weak interaction cross sections.

We will now examine the rate of change of the particle densities for the same set of τ values. In Table 2, we show the totals summing over all the energy bins for each particle. During the simulation, we track separately each particle's positive rate, the rate at which the density is increased (appears on the RHS of a reaction), and its negative rate which is the rate at which the density decreases (LHS of a reaction). The values shown are the rates per second divided by the initial neutron density. To obtain the total rates for a volume of 1 m^3, multiply by $n_{0,n}$ which, in this case, is 10^{41}. To obtain the rates per unit τ, multiply by $t_n/10^{18} = 4.3\times10^{-23}$.

We see that the $e^{\pm}$ and photon patterns are very similar. For the earlier values of time, there is a net gain of the same order of magnitude as the positive and negative rates. Later, however, while the positive and negative magnitudes have remained unchanged, the net has dropped by many orders of magnitude.

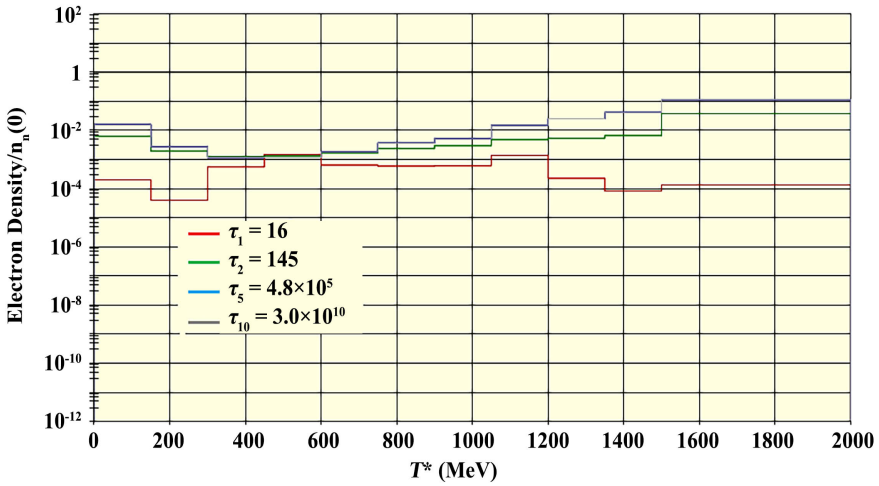

Figure 12. Electron energy distributions for four values of τ.

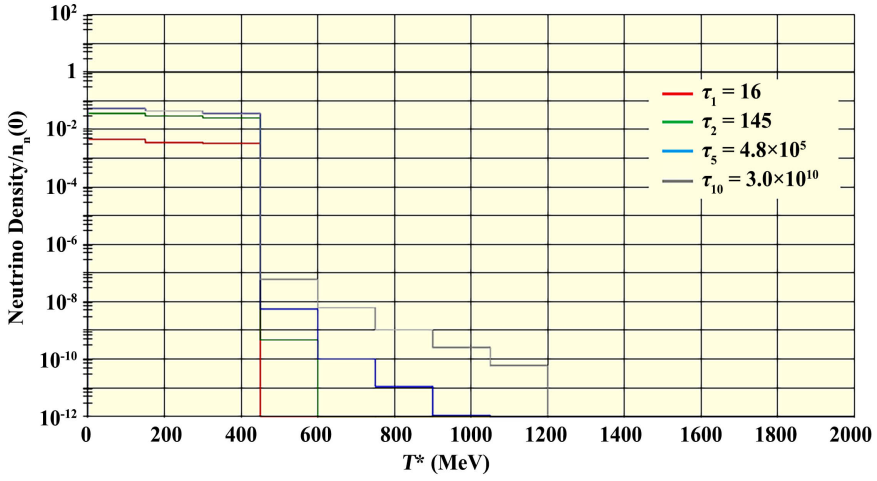

Figure 13. Neutrino energy distributions for four values of τ.

Table 2. Particle density change rates for 4 values of τ.

	$\tau = \tau_1$			$\tau = \tau_2$		
	Pos	Neg	Net	Pos	Neg	Net
e^-, e^+	3.2×10^{19}	1.2×10^{19}	2.0×10^{19}	2.5×10^{20}	2.4×10^{20}	9.4×10^{18}
$\nu, \bar{\nu}$	3.7×10^{19}	6.3×10^{5}	3.7×10^{19}	5.0×10^{18}	6.5×10^{5}	5.0×10^{18}
$n, \bar{n}$	3.8×10^{20}	8.4×10^{20}	-4.6×10^{20}	1.2×10^{19}	2.8×10^{19}	-1.6×10^{19}
$p, \bar{p}$	5.8×10^{19}	3.7×10^{19}	2.2×10^{19}	4.6×10^{18}	6.2×10^{18}	-1.7×10^{18}
γ	8.7×10^{20}	2.4×10^{19}	8.4×10^{20}	3.4×10^{20}	3.2×10^{20}	1.7×10^{19}
	$\tau = \tau_5$			$\tau = \tau_{10}$		
e^-, e^+	1.2×10^{21}	1.2×10^{21}	4.1×10^{11}	1.2×10^{21}	1.2×10^{21}	2.5×10^{12}
ν $\bar{\nu}$	9.0×10^{11}	2.8×10^{2}	9.0×10^{11}	1.2 0.6	0.18 0.1	1.0 0.5
$n, \bar{n}$	9.8×10^{11}	1.9×10^{12}	-9.6×10^{11}	1.9×10^{5}	1.9×10^{5}	0.6
$p, \bar{p}$	1.9×10^{12}	2.7×10^{12}	-8.3×10^{11}	9.3×10^{8}	9.3×10^{8}	−0.6
γ	9.7×10^{20}	9.7×10^{20}	2.0×10^{12}	9.7×10^{20}	9.7×10^{20}	-5.1×10^{12}

With the baryons, the positive, negative, and net magnitudes are similar but have decreased by several orders of magnitude by $\tau = \tau_5$ as a result of the annihilations. The rates for neutrons and protons are similar for the earlier times but by $\tau = \tau_{10}$, the positive and negative rates for the protons are three orders of magnitude larger than those of the neutrons as a result of the lepton and photon elastic scattering reactions. The net rates for the two, on the other hand, are of the same order of magnitude.

Referring now to the neutrinos, for the first three times, the positive rates are dominated by the baryon annihilation reactions. The very much smaller negative rates are a result of the weak reactions. By $\tau = \tau_{10}$, the rates are all small and are entirely a result of the weak interactions since the annihilation reactions have ceased. Notice that the weak interaction net rates are no longer much different from the net rates of the protons and neutrons. The reason for this is that, even though the densities of the baryons have dropped by a factor of 10^8 from their early values and the weak interaction cross sections are on the order of 10^{-42} m^2, the densities of the $e^{\pm}$ and neutrinos remain on the order of 10^{40} m^{-3}.

We will finish this section with a few comparisons between simulations with different parameters. First, we checked the sensitivity on the lepton elastic scattering cutoff angle and found only small changes in the $e^{\pm}$ and neutrino densities. We next did a run with 17 bins per particle instead of 12 with much the same results which was fortunate because increasing the bin count by that amount more than doubled the simulation run time.

The two principal parameters of the model are the initial neutron density and the neutron excess. In **Figure 14**, we show the $n_n(0) = 10^{42}$ m^{-3} results.

Comparing with Figure 8, we see that the process is compressed into a shorter period but otherwise the curves look the same. In other words, increasing the initial density by a factor of 10 did not affect the final *scaled* neutron and proton densities. The actual densities of all the particles are, of course, increased by a factor of 10.

We also ran a simulation with an initial neutron excess of 1.0×10^{-8} and obtained the results shown in Figure 15.

Aside from the final baryon densities, there are only a very few slight differences in the curves. The final baryon densities, however, are 1/2 the values found with a nucleon excess of 2.0×10^{-8}. The conclusion is that, at least in the range of densities considered, the final baryon densities vary in direct proportion to the initial neutron density and to the neutron excess.

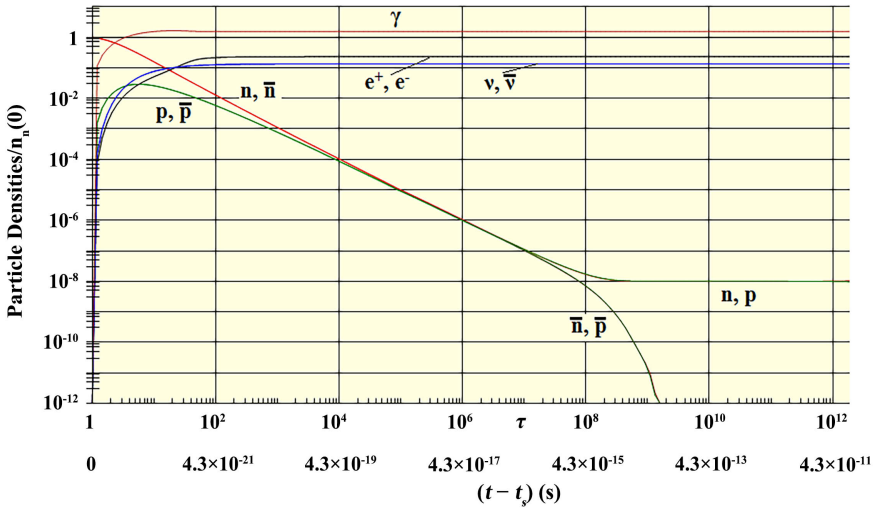

Figure 14. Simulation results with an initial neutron density $n_n(0) = 10^{42}\ \mathrm{m}^{-3}$ and a neutron excess of 2.0×10^{-8}.

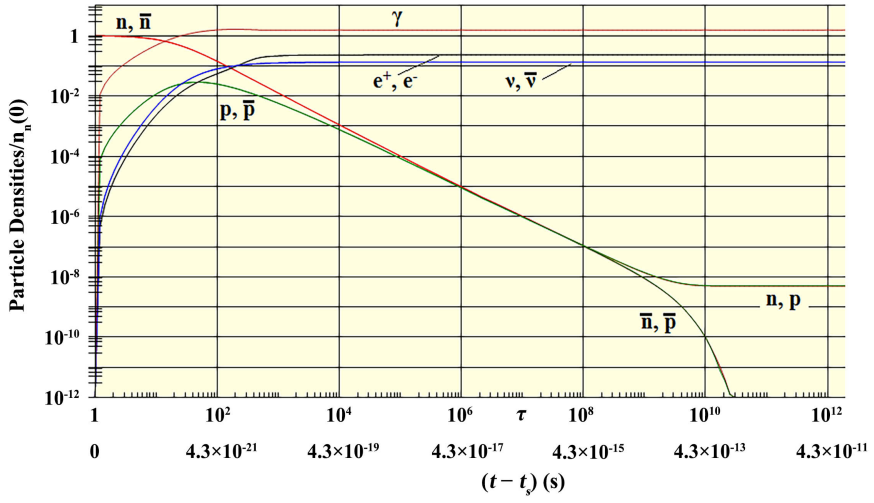

Figure 15. Simulation results with an initial neutron density $n_n(0) = 10^{41}\ \mathrm{m}^{-3}$ and a neutron excess of 1.0×10^{-8}.

6. Weak Interactions

From Table 2, we see that the weak reaction rates were very small during the early phases of the simulation and that they only begin to become comparable to the baryon reaction rates at $\tau = \tau_{10}$. As a check, we ran a simulation with the weak interactions turned off and the results were the same over the range of τ we have so far considered. The weak interactions are important, however, because they were responsible for the change in the p/n ratio from a value of unity at the end of the first phase to a value of 7.4 at the end of the second phase. In Figure 16, we show the simulation results extended to $\tau = 10^{16}$.

We find that the weak interactions begin to have a noticeable effect by a time of about $\tau = 10^{13}$. The p/n ratio is a long way from its final value and in fact, it has moved in the wrong direction, but it is no longer unity which indicates that the weak interactions are beginning to be of consequence.

The reason we do not see a predominance of protons at this point is that the CM energies of the weak reactions are much too large. In Figure 17, we show the energy distribution of the $n + e^+ \rightarrow p + \bar{\nu}$ reaction at $\tau = 10^{15}$.

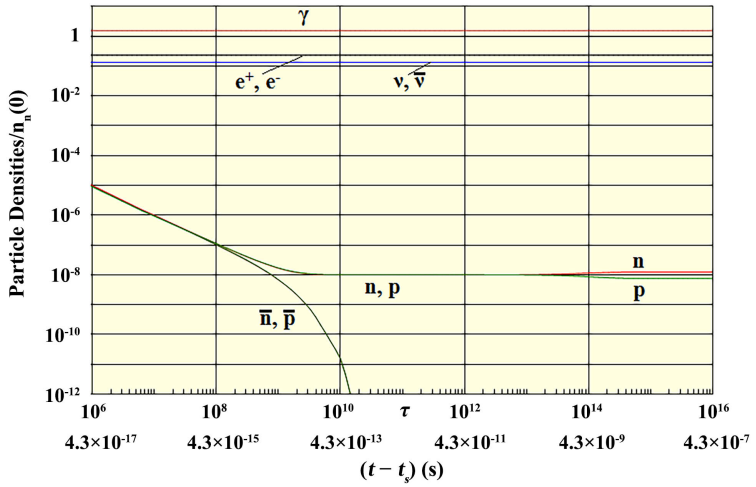

Figure 16. Simulation results with the same parameters as those in Figure 8.

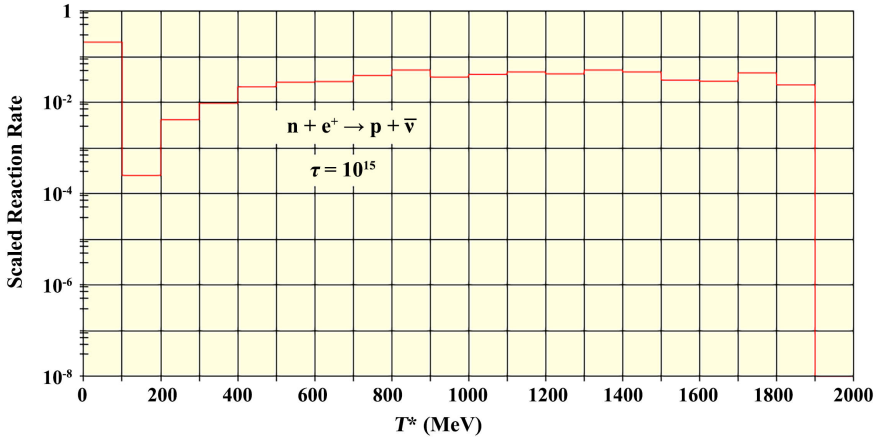

Figure 17. Scaled reaction rate for the $n + e^+ \rightarrow p + \bar{\nu}$ reaction at $\tau = 10^{15}$.

The $p+e^- \to n+\nu$ has an almost identical distribution. The rates of the $n+\nu \to p+e^-$ and $p+\bar{\nu} \to n+e^+$ reactions are a little lower but with similar distributions. At these energies, the cross sections for these reactions are the same aside from the factor of 1/2 for the $\bar{\nu}$ reactions. To achieve a value of $p/n = 7.4$, the p + lepton reaction cross sections must be smaller than the n + lepton cross sections by that same ratio and that could not have happened until the CM energies were very much smaller. Thermalization was partially responsible for the shift to lower energies but the expansion was also important. The first phase proceeded so rapidly that the size of the universe did not change but during the second phase, the scaling changed by a factor of $(4.3 \times 10^{-5}/0.135)^{-1/2}$ and since the kinetic energies of the protons and neutrons vary as the square of the scaling, their energies would have decreased by a factor of 3×10^4 by the time the third phase began.

According to [19], at the point in time when the temperature had dropped to a value of $kT = 1\,\text{MeV}$ and assuming thermal equilibrium, the n + lepton cross sections would have been on of order $\sigma = 10^{-15}$ mb, the positron density would have been $n(e^+) = 2.4\times10^{37}\ \text{m}^{-3}$, the electron/positron to neutrino abundance ratio of would have been $e^{\pm}/\nu = 2$, and the equilibrium p/n ratio, given by

$$p/n = e^{-\left(m_n c^2 - m_p c^2\right)/kT}, \tag{6-1}$$

would have been $p/n = 3.6$. The time at which this happened was $t = 0.056$ s.

We now compare with the simulation results. After starting with an initial density of $10^{41}\ \text{m}^{-3}$ and correcting for the expansion, the electron/positron density was $n(e^{\pm}) = 4.8\times10^{35}\ \text{m}^{-3}$ and the abundance ratio was about 1.7. These results are to some degree uncertain due to the issues discussed earlier concerning the annihilation branching ratios. The results are not exactly the same as the standard model results but they aren't radically different either. The situations, however, are completely different. The standard model assumes thermal equilibrium and does not concern itself about where the leptons came from. In this new model, the leptons are the product of the annihilation reactions so their number is determined by processes that had nothing to do with thermal equilibrium. There is no reason to suppose that the weak interactions ever did reach thermal equilibrium before the final phase of nucleosynthesis began. All that was necessary was that the particle energies drop to the point that the p + lepton reaction rates became much smaller than the n + lepton rates and whether or not thermal equilibrium was achieved is of no consequence.

What is clear is that because of the very small neutrino reaction cross sections, a very high density of $e^{\pm}$ and neutrinos must have existed and this model accounts for such populations naturally. This we view as a major success of the model.

7. Nucleosynthesis Proper

In [1], we outlined our theory of nucleosynthesis, listed the relevant reactions,

and presented results for a few different initial baryon densities. At that time, we did not have any firm basis for favoring one initial density over another. That situation has now changed as a result of our more recent work described in [3]. In that paper, we show how differences in the initial baryon densities led to the existence of all present-day cosmic structures including the voids. The standard model assumes that the content of the universe was initially uniform and, although it didn't happen, structure development was the result of accretion initiated by small perturbations. That model, however, cannot account for the voids because there is no such process as "unaccretion".

Discussions of the standard model generally begin with the statement that the universe is homogeneous and isotropic and then go on to develop a theory with a single value of the parameters. The result is that the outcome of nucleosynthesis would be the same everywhere. The universe is indeed homogeneous and isotropic on very large scales. If, for example, observers were dropped into the universe at different locations, the universe would appear to be the same to all of them. The corner store for one might be green and for another, red, but the general pattern of streets and buildings would be the same. The colors illustrate the point that on smaller scales, and galaxies are within the definition of smaller scales, the universe is *not* homogeneous and isotropic so one cannot base a theory of nucleosynthesis on the assumption that it is. Doing so leads to the problem researchers have in trying to discover the single initial baryon density that will reconcile the observed differences in the abundances of the various light elements when the fact is that there was no single baryon density.

In [3], we showed that all cosmic structures were defined during nucleosynthesis by regions with different initial baryon densities. In the regions that later became galaxies, for example, the average baryon densities ranged from 10 to 20 times the background average density depending on the mass and size of the galaxy. Further, there would have been variations within those regions. From our study of galaxy cluster evolution, [20], we determined that a general decrease in the average density within a structure from the center toward the outer boundary must have existed to prevent a free-fall collapse. The region is further separated into subregions that later became the stars, galactic bulges, spiral arms, and so forth. At the time of nucleosynthesis, stars were not the compact objects we see today. Instead, in their proto-form, they occupied regions that collectively nearly filled the galaxy with only shallow valleys separating one star from another.

In what follows, we refer to densities at the time of nucleosynthesis in terms of their present-day equivalent densities (PDED.) For example, the average baryon density is about 1 m^{-3} at present which corresponds to a density of $2.2\times10^{28}\ \mathrm{m}^{-3}$ at $t=0.135\ \mathrm{s}$. The PDED is defined by $\mathrm{PDED}\equiv\rho\left(t_{nuc}\right)\left(a\left(t_{nuc}\right)/a\left(t_0\right)\right)^3$ where $\rho\left(t_{nuc}\right)$ is the density at some location *at the time* of nucleosynthesis and $a(t)$ is the scaling. The PDED is *not* representative of the density within any present-day structure. The average PDED of the Milky Way at the time of nuc-

leosynthesis, for example, was about 17 m^{-3}. What that means is that the region that eventually became the galaxy, which had *coordinate* dimensions many times larger than the present-day size of the galaxy had an average density of 17 times 2.2×10^{28} m^{-3}. For a dwarf galaxy, a typical value is 10 m^{-3}. The reason for using this scheme is that it is much easier to appreciate that a region with a PDED of 17 had a density 17 times greater than the background than it would be by working with a value of 3.7×10^{29} m^{-3}.

As a starting point, we show in **Figure 18**, the simulation results for a PDED of 1 m^{-3}.

In this case, the mass ratio of ^{4}He is 0.234. Discussions of the abundances of the other species, on the other hand, typically refer to abundance ratios instead of mass ratios. The values are

$$^4\mathrm{He}/\mathrm{H} = 0.0772 \tag{7-1a}$$

$$\mathrm{D}/\mathrm{H} = 4.70\times10^{-4} \tag{7-1b}$$

$$^3\mathrm{He}/\mathrm{H} = 2.72\times10^{-5} \tag{7-1c}$$

$$^7\mathrm{Li}/\mathrm{H} = 2.50\times10^{-10}\,. \tag{7-1d}$$

Another parameter commonly used is $A(\mathrm{Li}) = 12 + \log_{10}(\mathrm{Li}/\mathrm{H})$ which, in this case, has a value of $A(^7\mathrm{Li}) = 2.4$.

Our goal is to relate differences in observed element abundances to differences in structure densities. To do this, we need to know how element abundances vary with baryon density which we discovered by running simulations over a range of initial densities. The curves in **Figure 19** are the result.

The usual practice is to use the photon/baryon ratio as the independent variable. It is a fact, however, that once the deuterium bottleneck has been passed, the photons no longer influence nucleosynthesis so the use of baryon density in the form of the PDED makes more sense.

To summarize, the ^{4}He abundance ratio is flat over much of the range shown but it does drop off sharply for small densities. The curve for ^{3}He is also fairly flat but again exhibits a drop for small densities. The deuterium density increases smoothly as the density drops whereas the abundance for ^{7}Li shows a peak at a PDED close to 1 and then rapidly declines. (When plotted against the photon/baryon ratio, the peak seen here becomes a valley.)

We will first look at the deuterium ratio. The gray band in the figure represents the range of values determined by a series of observations along lines of sight out to a distance of 100 pc from the Sun, [21]. From that same reference, for greater distances, the values range from $5\times10^{-6} \le \mathrm{D}/\mathrm{H} \le 22\times10^{-6}$. There have been numerous other determinations, [22], with results indicating considerably larger abundances up to as much as 3×10^{-4}. Each of these measurements claims good error statistics but the results are clearly inconsistent. This is a real problem for the single, universal nucleosynthesis model but is perfectly understandable in the new model.

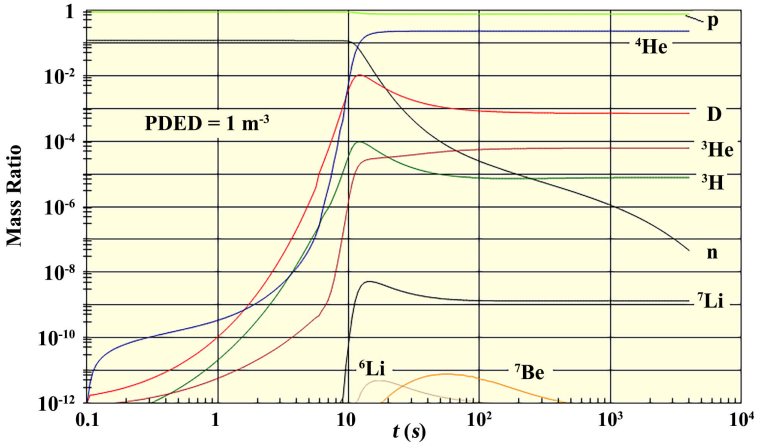

Figure 18. Simulation results for PDED = 1 m^{-3}.

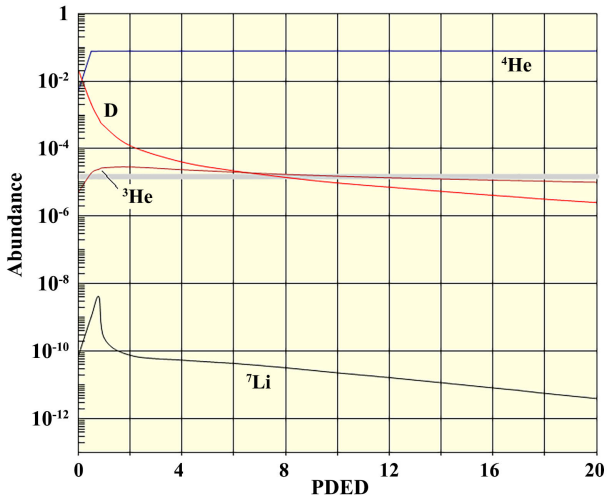

Figure 19. Abundance ratios as a function of PDED. The gray band is explained in the text.

According to our galaxy formation model, the Milky Way has an average $\text{PDED} \approx 17$. Referring to the figure, we see that for such a density, the deuterium density would have been much smaller than any of the reported values. But the value of 17 is an average representing the total mass of the galaxy which includes the stars, the interstellar medium, and the vacuum energy excess that is the reality of dark matter. The reactions, on the other hand, are only dependent on the particle densities at the locations where the reactions were happening. In this case, the observations were made along lines of sight through the interstellar medium and those regions at the time of nucleosynthesis would have generally had equivalent baryon densities considerably smaller than the overall average value of 17. In addition, the Solar System exists in what is known as the Local Bubble which has a lower density than the surrounding regions. It is no surprise, then, that the density of about 8 that corresponds to the results reported in [21] has a value is about 1/2 the average value. We also see the lowest density reported corresponds to $\text{PDED} \approx 15$ which is not much different from the aver-

age for the galaxy as a whole.

Referring to the large abundance results, to obtain a ratio on the order of 10^{-4}, a value of $\text{PDED} \approx 2$ is required. Unlike the results reported in [21], however, the large abundance results were obtained from observations of Lyman-α sources remote from any galaxies so densities close to the average density of the universe would be expected. All this indicates that the inconsistency of the observed abundances is just a matter of the existence of different densities *at the time of nucleosynthesis* between one region and another.

The abundance ratio of ^{4}He is nearly independent of the baryon density for densities larger than $\text{PDED} \approx 0.5$ so it is not surprising that determinations of the primordial abundance are consistent despite the density variations that existed during nucleosynthesis. The only exception is for regions with a very low density such as within the Boötes void. In **Figure 20**, we show the simulation results for a $\text{PDED} \approx 0.016$.

In this case, protons completely dominate the distribution with the density of ^{4}He falling below that of deuterium. Actual observations of these ratios would be difficult, however, because of the very low densities and contamination from higher density regions surrounding the void.

There is not much that can be said about ^{3}He because this element leads a very active life inside stars making it difficult to impossible to identify regions with primordial populations. The authors of [23] report a value of $^3\text{He}/\text{H} = 1.6 \pm 0.5 \times 10^{-5}$ which is consistent with the simulation results but the jump from the measured ratio to a primordial abundance is problematic.

We will finish with ^{7}Li. The best estimates of the primordial abundance of ^{7}Li are obtained from observation of metal-poor halo stars located in the outer regions of the Milky Way. The values fall in the range $2.1 \le A\left(^7\text{Li}\right) \le 2.3$ which implies a value of PDED a little less than 1. Referring to our model, it is expected that the baryon density in the outer regions of the proto-galaxy would be less on average than in the interior so the material making up the halo stars would have had a higher abundance of ^{7}Li than regions closer to the center of the galaxy.

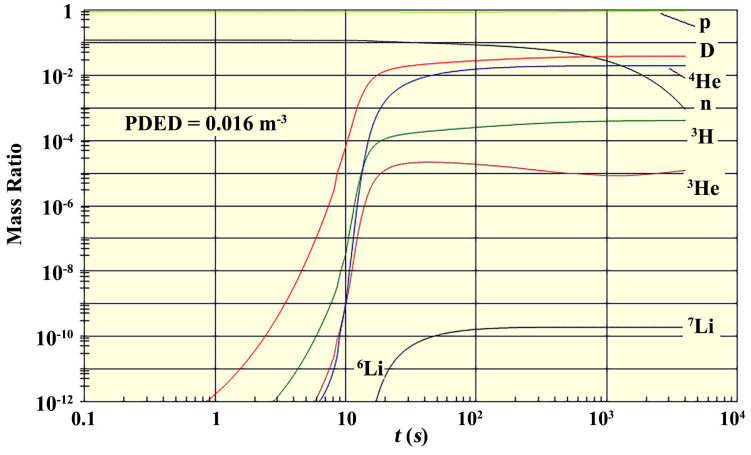

Figure 20. Nucleosynthesis in a region with very low baryon density.

Summing up, we find that our new model of galaxy formation can readily account for the variations in the initial baryon densities needed to explain the observed abundances of the light elements and, in doing so, shows why one-size-fits-all nucleosynthesis will fail. We also see that the range of densities is consistent with the values predicted by our model of galaxy (and star) formation. At this stage, we can't make precise numerical predictions so these results are only suggestive. To obtain precise predictions, we would need to conduct simulations on a scale far beyond what can be managed on a laptop.

8. CMB

Earlier we stated that the photons created by the annihilation reactions became the CMB. To substantiate that claim, we need to show that the photon gas has all the right characteristics.

We will first show that the photons have the right temperature. There are a couple of ways we can estimate the temperature of the photon gas. One way is to calculate the total number of photons by summing the bin counts and the total energy by summing for each bin, the product of its count by its center energy. We then calculate the temperature by dividing the two results and setting this to the black-body formula, $E_T/N_T = \pi^4/\left(30\zeta\left(3\right)\right)kT$. Choosing a time of $\tau = 10^{12}$, for example, we obtain a temperature of $T_{Sim} = 6.9\times10^{11}$ K.

This problem with this method is that, although the total energy is meaningful, the distribution of the photons among the bins did not yet reflect a black-body distribution so a method that avoids using the photon bin counts should give a better result. The formula for the total energy of a black-body photon gas is,

$$E/V = \frac{8\pi^5}{15\left(hc\right)^3}\left(kT\right)^4 \tag{8-1}$$

and substituting the total energy gives a value of $T = 2.7\times10^{11}$ K. The actual value of the CMB obtained from the present-day CMB temperature is $T_{CMB}\left(t_n\right) = 4.3\times10^{11}$ K. The results are quite close. If we calculate the temperature using the results from the 10^{42} m^{-3} initial density simulation, we obtain a temperature of $T = 4.8\times10^{11}$ K. Based on the temperature alone, the photons produced by the annihilations certainly qualify as the CMB.

We next will consider the thermalization problem. To be able to compare the simulated photon energy distribution with the black-body distribution on an equal footing, we calculate the bin distribution for a photon gas with a black-body spectrum. The number density of a black body is given by

$$n\left(\nu\right) = \frac{8\pi\nu^2}{c^2}\frac{1}{\mathrm{e}^{h\nu/kT}-1}. \tag{8-2}$$

If we integrate this over the energy range of the bins,

$$n_{bin} = \frac{8\pi}{\left(hc\right)^3}\int_{E_{\min}}^{E_{\max}}\mathrm{d}E\,\frac{E^2}{\mathrm{e}^{E/kT}-1}, \tag{8-3}$$

we obtain the curve shown in **Figure 21**.

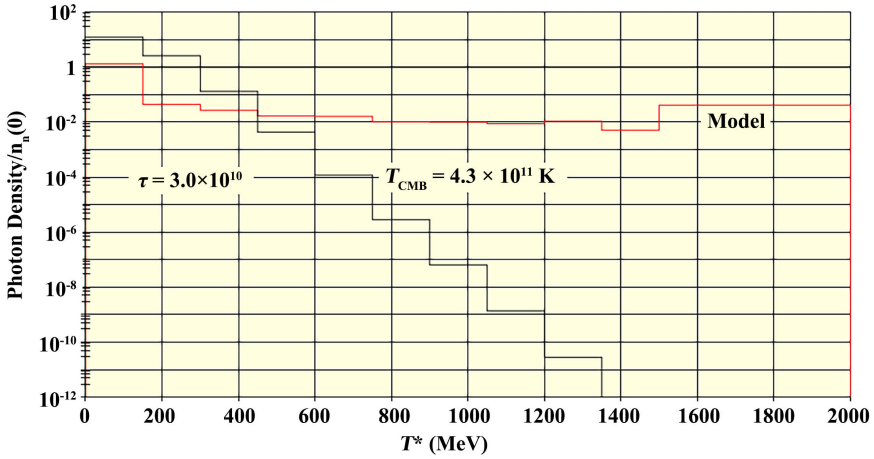

Figure 21. Comparison between the simulation photon energy distribution and blackbody distributions at the actual CMB temperature.

It is immediately clear that the model distribution is too flat. We have already seen that the photon reaction rates are very large so it is not a matter of nothing happening. The problem is that the system of particles has reached a non-blackbody equilibrium and even though the reaction rates are large, no energy transfer is taking place.

The root of the problem lies with the mesons we did not include in the simulation. The baryons are undergoing elastic scattering but that process has stabilized. There are also high rates of $e^{\pm}p$ scattering occurring in which energy from the protons is transferred to the electrons and then to the photons but because of the small mass of the electrons, there is no recoil of the protons. What is missing is a mechanism that extracts energy from the baryons and it is the neglected low-mass mesons that would do just that.

Elastic scattering of the mesons from the neutrons and protons would transfer energy away from the baryons but more important would be the multi-meson deep inelastic scattering reactions such as $p+p \rightarrow p+p+\text{mesons}$. Each such reaction would extract from the baryons, the energy equivalent of the masses of the mesons. The cross sections for these reactions increase with energy so they would act to shift the energy distribution of the baryons towards lower energies. From [16], we find that the cross section for the single pion production reaction, $n+p \rightarrow n+p+\pi^0$ at the relatively low incident proton energy of 580 MeV, has already reached a value of 10 mb which is about 40% of the elastic cross section. Shifting the protons to lower energies would immediately be reflected in the electron and photon energy distributions via the reactions mentioned earlier. The mesons would also provide a two-step feedback path by which the photons could transfer energy back to the baryons.

While we are confident that including the meson production reactions would explain the thermalization, to demonstrate that this idea is correct, we would need to include the mesons in the simulation along with a long list of meson production, scattering, and decay reactions. The reason we have not done so was

explained earlier; namely that the simulation run times would become prohibitively long.

Having suggested a solution to the thermalization problem, the final requirement is to account for the CMB anisotropy spectrum. The standard model asserts that the spectrum is a result of acoustic oscillations but we have shown in [1] that acoustic oscillations on the scale of superclusters are impossible because of causality. In our annihilation model, the energy of the photon gas is dependent only on the initial neutron density whereas the final baryon density is also a function of the neutron excess. The consequence is that we can achieve any desired final baryon density desired by varying either or both of the initial density or the neutron excess. Our feeling is that because the neutron excess must, in some way, reflect an as yet undiscovered fundamental property of QCD, its value will be fixed. Assuming that is the case, the differences in the PDED of various structures are solely a matter of different initial densities which, in turn, implies that the photon gas temperatures will also vary from one structure to another.

Taking again the Milky Way as an example, its PDED of 17 implies an initial neutron density 17 times greater than that of the background and as we have seen, this would result in photon gas energy also 17 times greater than the background. The temperature of the gas would then be $17^{1/4} = 2.0$ times the temperature of the background photons. On a different size scale, the Virgo galaxy cluster value is PDED = 2.5 which implies a temperature 1.3 times higher than the background. Conversely, in the void regions, the initial density was lower so the temperature would also be lower. We see that this model naturally accounts for anisotropy in the photon gas temperature distribution because the temperature distribution across the universe was determined by the mass distribution across the universe *during the first phase of nucleosynthesis*.

We now come to superclusters. According to our model, superclusters came into existence in the form of filaments built of regions of higher than average density which evolved into the member galaxy clusters and other structures. Because of their extreme size, the filaments do not evolve but the components making the filaments do. In [1], we argued that the superclusters were responsible for the observed CMB spectrum but the reality is that both are consequences of the same pattern of densities that were embedded in the vacuum energy at the time of the initial Plank-era inflation.

The remaining difficulty is that the predicted temperature variances are much too large. At the time of nucleosynthesis, they were of the same order of magnitude as the average temperature whereas the observed anisotropies of the CMB are smaller than the average temperature by a factor of about 10^{-5}. To some extent, averaging over the dimensions of the supercluster will reduce the anisotropy peaks but to complete the theory, we will need to perform a careful study that follows the evolution of the photon gas from its inception at the time of nucleosynthesis up to the time of recombination when the anisotropy distribution was frozen by the decoupling of the photons from matter. The significant advance we

present here is that knowledge of the origin of the anisotropies opens up the possibility of being able to calculate the observed amplitude of the spectrum at the time of recombination.

9. Conclusions

In our original paper describing a new model of cosmology, we proposed a model of nucleosynthesis based on the idea that the matter content of the universe came into existence when a small percentage of the vacuum energy underwent neutron-antineutron pair production with a very small density of extra neutrons. In this paper, we examined that idea in detail and found that our original idea was correct. The annihilation model accounts for the baryonic matter/antimatter asymmetry and total baryon content of the universe. In addition, it predicts a photon gas abundance in agreement with present-day CMB temperature and also explains the origin of the CMB anisotropy spectrum. The same processes result in very high densities of both $e^{\pm}$ and neutrinos with abundances in reasonable agreement with the thermal equilibrium abundances required by the standard model.

The principal shortcoming of this work is our failure to accurately represent the various branching channels of the annihilation reactions. This failure prevents keeps us from simulating the thermalization of the baryons and photons and it also limits the accuracy of the lepton abundance predictions. These, however, do not affect the baryon abundance calculations so the accuracy of the principal predictions of the model is limited only by the cross-section extrapolations.

We showed that variations in the initial density of neutrons were responsible for the existence of all cosmic structures including the voids and that these same variations account for the differences between observed densities of the abundances of the light elements which are impossible to explain using a universal, single-density model of nucleosynthesis.

Conflicts of Interest

The author declares no conflicts of interest regarding the publication of this paper.

References

[1] Botke, J.C. (2020) A Different Cosmology: Thoughts from Outside the Box. *Journal of High Energy Physics, Gravitation and Cosmology*, **6**, 473-566. https://doi.org/10.4236/jhepgc.2020.63037

[2] Greene, G.L. and Geltenbort, P. (2016) The Neutron Enigma. *Scientific American*, **314**, 36-41. https://doi.org/10.1038/scientificamerican0416-36

[3] Botke, J.C. (2021) The Origin of Cosmic Structure, Part 1—Stars to Superclusters. *Journal of High Energy Physics, Gravitation and Cosmology*, **7**, 1373-1409. https://doi.org/10.4236/jhepgc.2021.74085

[4] Møller, C. (1945) General Properties of the Characteristic Matrix in the Theory of

Elementary Particles I. *Det kongelige Danske videnskabernes selskab matematisk-fysiske Meddelelser*, **23**, 48 p.
http://gymarkiv.sdu.dk/MFM/kdvs/mfm%2020-29/mfm-23-1.pdf

[5] Brückner, W., Cujec, B., Döbbeling, K., *et al.* (1989) Measurements of the Antiproton-Proton Annihilation Cross-Section in the Beam Momentum Range between 180 and 600 MeV/c. CERN-EP/89-105.
https://cds.cern.ch/record/200305/files/cer-000111954.pdf

[6] Bressanni, T. and Filipppi, A. (2003) Antineutron Physics. *Physics Reports*, **383**, 213-297. http://www.ph.unito.it/ccl/docenti/menichetti/CIVR/bressani.pdf
https://doi.org/10.1016/S0370-1573(03)00233-3

[7] Hamilton, R.P., Pun, T.P., Tripp, R.D., Nicholson, H. and Lazarus, D.M. (1980) Measurement of the Anti-*pp* Charge Exchange Cross-Section from 0.119 to 1.046 GeV/c. *Physical Review Letters*, **44**, 1179-1181.
https://journals.aps.org/prl/abstract/10.1103/PhysRevLett.44.1179
https://doi.org/10.1103/PhysRevLett.44.1179

[8] Brückner, W., Döbbeling, H., *et al.* (1986) Measurement of the $\bar{p}p \to \bar{n}n$ Cross Section as Low $\bar{p}$ Momenta. *Physics Letters B*, **169**, 302-308.
https://www.sciencedirect.com/science/article/abs/pii/0370269386906714
https://doi.org/10.1016/0370-2693(86)90671-4

[9] Linssen, L. (1986) The Measurement of Antiproton-Proton Total Cross Sections and Small-Angle Elastic Scattering at Low Momenta. Ph.D. Thesis, University of Amsterdam, Amsterdam.
https://inis.iaea.org/collection/NCLCollectionStore/_Public/18/025/18025994.pdf

[10] Abe, K., Adam, J., Aihara, H., *et al.* (2015) Measurement of the ν_μ Charged Current Quasi-Elastic Cross-Section on Carbon with the T2K On-Axis Neutrino Beam. arXiv:1503.07452v2. https://arxiv.org/pdf/1503.07452.pdf

[11] Particle Data Group (2019) 50. Neutrino Cross Section Measurements.
https://pdg.lbl.gov/2019/reviews/rpp2019-rev-nu-cross-sections.pdf

[12] Gamma-Ray Cross Section. Wikipedia.
https://en.wikipedia.org/wiki/Gamma_ray_cross_section

[13] Rieger, F. (n.d.) High Energy Astrophysics—Lecture 10.
https://www.mpi-hd.mpg.de/personalhomes/frieger/HEA10.pdf

[14] Møller Scattering. Wikipedia.
https://en.wikipedia.org/wiki/M%C3%B8ller_scattering

[15] Thomson, M. (2009) Particle Physics. Handout 5: Electron-Proton Elastic Scattering.
https://www.hep.phy.cam.ac.uk/~thomson/lectures/partIIIparticles/Handout5_2009.pdf

[16] Dzhelepov, V.P., Golovin, B.M., Kazarinov, I.M. and Semenov, N.N. (1958) Elastic Scattering of 580 MeV Neutrons by Protons and Neutrons. CERN Report, 115-124.
https://cds.cern.ch/record/1241659/files/p115.pdf

[17] Adlarson, P., Augustyniak, W., Bardan, W., *et al.* (2020) Differential Cross Sections for Neutron-Proton Scattering in the Range of the d*(2380) Dibaryon Resonance. *Physical Review C*, **102**, Article ID: 015204. https://arxiv.org/abs/2003.13057

[18] Brückner, W., Cujec, B., Döbbeling, H., *et al.* (1991) Measurements of the Antiproton-Proton Elastic Cross Section in the Beam Momentum Range between 180 and 600 MeV/c. CERN-PPE/91-41. http://cds.cern.ch/record/218245
https://doi.org/10.1007/BF01560639

[19] Hirata, C. (2008) Big Bang Nucleosynthesis: Overview.

https://www.tapir.caltech.edu/~chirata/ph217/lec05.pdf

[20] Botke, J.C. (2022) The Origin of Cosmic Structure, Part 3—Supermassive Black Holes and Galaxy Cluster Evolution. *Journal of High Energy Physics, Gravitation and Cosmology*, **8**, 345-371. https://doi.org/10.4236/jhepgc.2022.82028

[21] Linsky, J.L. (2003) Atomic Deuterium/Hydrogen in the Galaxy. *Space Science Reviews*, **106**, 49-60. https://arxiv.org/abs/astro-ph/0309099

[22] Olive, K.A., Steigman, G. and Walker, T.P. (2000) Primordial Nucleosynthesis: Theory and Observations. *Physics Reports*, **333**-**334**, 389-407. https://arxiv.org/abs/astro-ph/9905320 https://doi.org/10.1016/S0370-1573(00)00031-4

[23] Balser, D.S., Bania, T.M., Rood, R.T. and Wilson, T.L. (1999) ^{3}He in the Milky Way Interstellar Medium Abundance Determinations. *The Astrophysical Journal*, **510**, 759-783. https://ui.adsabs.harvard.edu/abs/1999ApJ...510..759B/abstract https://doi.org/10.1086/306598